Enhanced Accuracy in Magnetic Actuation: Closed-Loop Control of a Magnetic Agent With Low-Error Numerical Magnetic Model Estimation

Onder Erin , *Member, IEEE*, Suraj Raval , *Student Member, IEEE*, Trevor J. Schwehr , Will Pryor,
Yotam Barnoy, Adrian Bell , Xiaolong Liu , Lamar O. Mair , Irving N. Weinberg , *Member, IEEE*,
Axel Krieger , *Member, IEEE*, and Yancy Diaz-Mercado , *Member, IEEE*

Abstract—**Magnetic actuation holds promise for wirelessly controlling small, magnetic surgical tools and may enable the next generation of ultra minimally invasive surgical robotic systems. Precise torque and force exertion are required for safe surgical operations and accurate state control. Dipole field estimation models perform well far from electromagnets but yield large errors near coils. Thus, manipulations near coils suffer from severe (10x) field modeling errors. We experimentally quantify closed-loop magnetic agent control performance by using both a highly erroneous dipole model and a more accurate numerical magnetic model to estimate magnetic forces and torques for any given robot pose in 2D. We compare experimental measurements with estimation errors for the dipole model and our finite element analysis (FEA) based model of fields near coils. With five different paths designed for this study, we demonstrate that FEA-based magnetic field modeling reduces positioning root-mean-square (RMS) errors by 48% to 79% as compared with dipole models. Models demonstrate close agreement for magnetic field direction estimation, showing similar accuracy for orientation control. Such improved magnetic modelling is crucial for systems requiring robust estimates of magnetic forces for positioning agents, particularly in force-sensitive environments like surgical manipulation.**

Index Terms—**Closed-loop control, magnetic modeling, magnetic robots, medical robotics.**

I. INTRODUCTION

RECENT advances in robotic surgery continue to improve surgical quality and in many cases clinical outcomes [1], [2]. Smaller surgical tools reduce surgical trauma considerably, improving recovery time and minimizing cosmetic effects of an intervention. Since traditional robotic surgical systems require a mechanical connection between robotic manipulators and surgical tools, miniaturization remains challenging.

Magnetic actuation is a promising alternative, untethering the surgeon from the surgical instrument. For procedures such as surgical suturing, magnetic actuation may enable ultra minimally invasive surgeries accomplished by decreasing the number and sizes of surgical ports [3], [4].

Magnetic actuation systems consist of custom-built electromagnetic coils or external permanent magnets [5] and can be used to exert forces and torques on magnetic surgical tools. Wireless capsule endoscopy [6], [7], magnetic suturing [4], [8], biopsy [9], [10], and magnetic catheter steering for various procedures [11]–[13] require a robust control of the magnetic agent with well-estimated torque and force exertion for safe and accurate operation.

Magnetic torque and force estimates require accurate modelling of the magnetic fields and gradients for predicting the position and pose of a magnetic agent, with the eventual goal of enabling surgical procedures to be performed under magnetic guidance. Commonly used magnetic dipole models only provide reliable force and torque estimates far from magnetic field sources [14], becoming increasingly inaccurate close to field sources. Moreover, to benefit from stronger magnetic actuation forces and torques, custom magnetic setups are compactly designed so as to minimize distances between magnetic agents and field sources [6], [8]. Compact design enables larger force exertion and further miniaturization of the magnetic agents, but also moves agents close to magnetic field sources, amplifying inaccuracies from magnetic dipole model based estimates. In such cases, controllers sensitive to modelling errors, such as model-based controllers, require (1) physically unrealistic tuning parameters, (2) confining workspace to a small region distant from the magnets, or (3) generating inaccuracies in simultaneous position and orientation control of an agent [15]–[17].

Various studies have estimated magnetic fields more accurately. Single-point-based one-dimensional dipole moment scaling [18], [19], mathematical model-based calibration with experimental magnetic field measurements [14], spline-based and Zernike polynomial-based fittings [17], [20], and control-oriented magnetic field mapping methods [21] have been explored. However, these approaches either cover only a limited part of the workspace, or focus on the theoretical and simulation aspects with limited study on experimental outcomes including lack of demonstration of simultaneous position and orientation control in the entire workspace.

This study has three main objectives. First, we aim to improve dipole model magnetic field estimation accuracy by developing a finite element analysis (FEA) based magnetic field estimation approach. Second, we aim to integrate the FEA-based magnetic field estimation by creating a look-up table for real-time closed-loop control. Lastly, we compare the autonomous control performance between the algorithms integrated with two different magnetic field estimation approaches. Importantly, we perform experimental evaluation of model performance for simultaneous position and orientation control (2D position, 1D orientation) on a flat surface, comparing two different magnetic field estimation methods. As the outcome of these studies, autonomous control of the robot throughout the whole workspace and experimental path-tracking performance improvements for five different paths are provided. The presented FEA-based magnetic field estimation would be beneficial for any magnetic actuation system to improve the experimental control performance, which could lead to more accurate force and torque exertion, possibly enhancing the safety and sensitivity of magnetic surgical systems.

II. EXPERIMENTAL SETUP AND MAGNETIC AGENT

A. High-Level System Components

The MagnetoSuture^{TM} system (Fig. 1) consists of (1) set of electromagnetic coils (custom-built), (2) power supply (Mean Well, RSP-1600-27), (3) microcontroller (Arduino Uno), (4) motor drivers (BasicMicro, Roboclaw 2x60AHV), (5) dedicated CPU (Acer Predator PH315-53, i7 10750H, RTX 2060), (6) video camera (FLIR BFS-U3-13Y3), and (7) a water cooling system with a pump (Little Giant 518087 1-EA-42). The power supply is rated at 27 V and 59 A, and was used to power electromagnetic coils via the motor drivers. The camera and the microcontroller continuously communicate with the dedicated CPU. The dedicated CPU is responsible for (1) receiving camera images, (2) processing images to localize the magnetic agent [16], (3) computing input currents required to achieve the desired agent motion, and (4) commanding the necessary pulse-width-modulation (PWM) signals to the microcontroller. The microcontroller uses the PWM signals to activate the motor drivers, which in turn power the coils. Each electromagnet has a dedicated motor driver channel, enabling independent coil control.

B. Electromagnetic Setup

Wireless magnetic actuation in the MagnetoSuture^{TM} setup is realized by four orthogonal electromagnetic coils located at
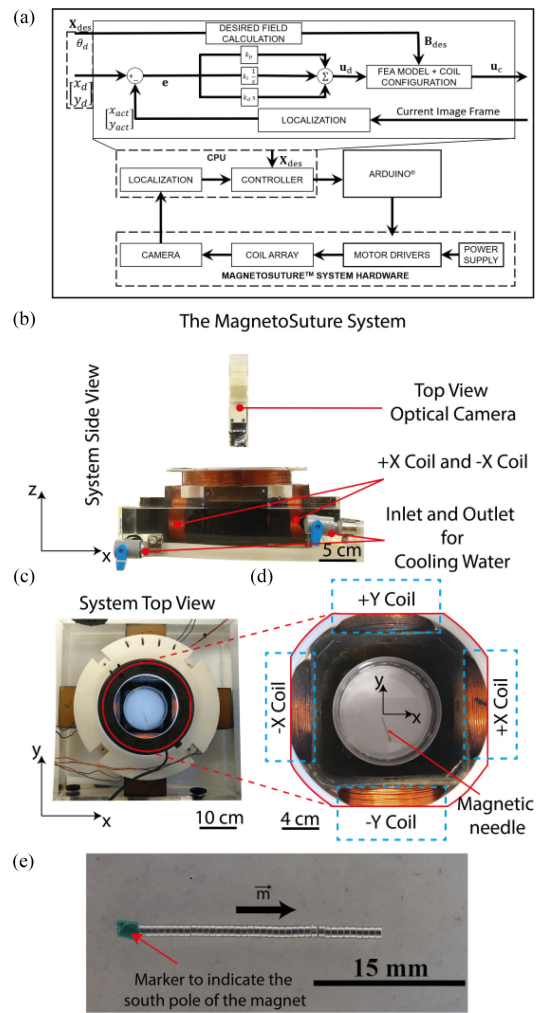

Fig. 1. The MagnetoSuture^{TM} system, consisting of an array of 4 coils surrounding a central Petri dish. a) High-level depiction of the mechatronic components and PID control block diagram. b) A side view of the system. The camera at the top allows for real-time magnetic agent localization and recording of experiments. c) Top view from camera. d) The four coils surround the dish in the cardinal directions, enabling actuation of a magnetic field by powering the coils. e) The magnetic agent has a cylindrical needle-like shape and is magnetized axially. The green marker facilitates detection of the south pole of the magnet.

the each end along $x-$ and $y-$ axes. Coils are designed to be identical in terms of material, windings, and geometry. Coils have outer diameters of 98 mm and lengths of 60 mm, with a total of 648 windings (AWG 18 magnet wire), resulting in 2.7 Ω resistance. The workspace region (cube, 10 cm on a side) at the center of these coils contains a Petri dish (85 mm diameter). The power supply is shared amongst the electromagnets. The maximum magnetic field strength generated by each electromagnetic coil at the center of the workspace is measured to be 28 mT. Further details have been previously reported in [8].

C. Magnetic Agent

Our magnetic agent is designed to represent a straight, 20 G hypodermic suture needle shape. We use a cylindrical magnetic agent 22 mm long and 1 mm in diameter. The agent is built from short, axially magnetized NdFeB disks (1 mm diameter, 0.5 mm

length, SuperMagnetMan D0106-50, N52) In total, 44 of these magnets are assembled axially to make up the magnetic agent. The overall magnetic dipole strength of the magnet is 2.0×10^{-5} kA-m^2, as calculated based on manufacturer's specifications for N52 grade NdFeB materials. Due to agent symmetry, a green adhesive marker attached at one end of the agent aids in orientation detection. The magnetic agent along with a high-level depiction of the physical experimental setup is shown in Fig. 1. The magnetic agent is placed in the Petri dish and completely submerged in glycerin (with $\sim$0.1% dish soap). Our glycerin with soap formulation is effective at minimizing stiction across all samples. All experiments are performed using the same magnetic agent, Petri dish, and fluid environment.

III. FUNDAMENTAL BACKGROUND

A. Magnetic Forces and Torques on the Robot

A ferrous object under magnetic fields experiences magnetic force, $\mathbf{F}_m$, and torque, $\boldsymbol{\tau}_m$, on its body. These actuation forces and torques are proportional to the object's magnetization vector. In what follows, we focus on a planar description of the electromagnetic force and torque experienced by a robot that contains a hard magnetic component. The closed-form force and torque equations of a magnetic object with magnetization vector, $\Psi_m \in \mathbb{R}^2$, under magnetic field vector, $\mathbf{B} \in \mathbb{R}^2$, can be represented as

$$\boldsymbol{\tau}_m = -v_m(\Psi_m^T \mathbb{S} \mathbf{B}), \tag{1}$$

$$\mathbf{F}_m = v_m(\Psi_m \cdot \nabla)\mathbf{B}, \tag{2}$$

where v_m is the volume of the magnetic component, and $\mathbb{S} = \begin{bmatrix} 0 & -1 \\ 1 & 0 \end{bmatrix}$. For an accurate estimation of exerted forces and torques on the magnet, the magnetic field vector, $\mathbf{B}$, and its spatial distribution should be estimated accurately. The dipole model is commonly used to estimate magnetic fields from coils and permanent magnets used in object manipulation. The dipole model assumes that the magnetic field is generated at single point in space – a particle with polarity. Even though this model can accurately capture the magnetic field generated from a coil at points that are at large distance from the source, the model becomes increasingly inaccurate as magnets approach the coil.

In our MagnetoSuture$^{\text{TM}}$ setup, we have four independently powered coils. The coil current vector is denoted by $\mathbf{u_C} = [i_1, i_2, i_3, i_4]^T$. The resultant magnetic field at a point $\mathbf{P} \in \mathbb{R}^2$ is

$$\mathbf{B_r}(\mathbf{u_C}, \mathbf{P}) = \sum_{k=1}^{4} \mathbf{B_k}(i_k, \mathbf{P}). \tag{3}$$

For each coil, the magnitude of the generated magnetic field scales linearly with the current in that coil. Thus, for any point $\mathbf{P}$, a linear operator with units of Tesla per ampere can be computed a priori and multiplied by the currents at the specific coil. Hence, (3) can be represented as

$$\mathbf{B_r}(\mathbf{u_C}, \mathbf{P}) = \begin{bmatrix} \bar{\mathbf{B}}_1(\mathbf{P}) & \bar{\mathbf{B}}_2(\mathbf{P}) & \bar{\mathbf{B}}_3(\mathbf{P}) & \bar{\mathbf{B}}_4(\mathbf{P}) \end{bmatrix} \mathbf{u_C} = \bar{\beta}(\mathbf{P})\mathbf{u_C} \tag{4}$$

where the matrix $\bar{\beta} \in \mathbb{R}^{2 \times 4}$ represents the magnetic field contribution from the electromagnetic coils per unit of current.

Similarly, the magnetic field gradient is the linear superimposition of the field gradients, and therefore, the magnetic pulling force, $\mathbf{F}_m$, can be represented as

$$\begin{bmatrix} \mathbf{F_{m_x}}(\mathbf{u_C}, \mathbf{P}) \\ \mathbf{F_{m_y}}(\mathbf{u_C}, \mathbf{P}) \end{bmatrix} = v_m \begin{bmatrix} \Psi_m^T \frac{\partial \bar{\mathbf{B}}_1(\mathbf{P})}{\partial x} & \cdots & \Psi_m^T \frac{\partial \bar{\mathbf{B}}_4(\mathbf{P})}{\partial x} \\ \Psi_m^T \frac{\partial \bar{\mathbf{B}}_1(\mathbf{P})}{\partial y} & \cdots & \Psi_m^T \frac{\partial \bar{\mathbf{B}}_4(\mathbf{P})}{\partial y} \end{bmatrix} \mathbf{u_C}. \tag{5}$$

For simultaneous position and orientation robot control, it is important to simultaneously establish both $\boldsymbol{\tau}_m$ and $\mathbf{F}_m$. In a planar system with four independent electromagnetic coils, it is possible to find a solution that satisfies $\mathbf{B_r}$ and $\mathbf{F}_m$ at the same time, so long as the magnetic fields are linearly independent. By combining (4) and (5), for the planar case in the xy plane, the system can be represented as

$$\begin{bmatrix} \tau_m \\ \mathbf{F}_m \end{bmatrix} = v_m \begin{bmatrix} -\Psi_m^T \mathbb{S} \bar{\beta}(\mathbf{P}) \\ \Psi_m^T \bar{\mathbb{G}}_\mathbf{x}(\mathbf{P}) \\ \Psi_m^T \bar{\mathbb{G}}_\mathbf{y}(\mathbf{P}) \end{bmatrix} \mathbf{u_C}, \tag{6}$$

where $\bar{\mathbb{G}}_\mathbf{x}$ and $\bar{\mathbb{G}}_\mathbf{y}$ are $\begin{bmatrix} \frac{\partial \bar{\mathbf{B}}_1(\mathbf{P})}{\partial x} & \frac{\partial \bar{\mathbf{B}}_2(\mathbf{P})}{\partial x} & \frac{\partial \bar{\mathbf{B}}_3(\mathbf{P})}{\partial x} & \frac{\partial \bar{\mathbf{B}}_4(\mathbf{P})}{\partial x} \end{bmatrix}$ and $\begin{bmatrix} \frac{\partial \bar{\mathbf{B}}_1(\mathbf{P})}{\partial y} & \frac{\partial \bar{\mathbf{B}}_2(\mathbf{P})}{\partial y} & \frac{\partial \bar{\mathbf{B}}_3(\mathbf{P})}{\partial y} & \frac{\partial \bar{\mathbf{B}}_4(\mathbf{P})}{\partial y} \end{bmatrix}$, respectively.

IV. 3-DOF CLOSED-LOOP CONTROL OF A MAGNETIC AGENT ON A PLANAR SURFACE

A. Closed-Loop Control Algorithm

Simultaneous position and orientation control of a magnetic agent on a planar surface is a multi-input multi-output (MIMO) system. The low level inputs are the four current values applied to the coils. The outputs of the system are the magnet's major-axis orientation, θ_{act}, and its planar position, (x_{act}, y_{act}). Here we denote the robot's current state as $\mathbf{X}_{\text{act}} = [x_{act} \ y_{act} \ \theta_{act}]^T$, and the desired state as $\mathbf{X}_{\text{des}} = [x_{des} \ y_{des} \ \theta_{des}]^T$.

To steer the robot from $\mathbf{X}_{\text{act}}$ to $\mathbf{X}_{\text{des}}$, both orientation and position of the robot should be controlled. To reflect the added benefit of accurate magnetic modeling with FEA-based simulations and to provide a contrast with the dipole model, a standard proportional-integral-derivative (PID) controller is selected for the implementation of the closed-loop position control, which can be represented as

$$\mathbf{u_d} = \begin{bmatrix} F_{x_{des}} \\ F_{y_{des}} \end{bmatrix} = k_p\mathbf{e} + k_i \int \mathbf{e}dt + k_d\dot{\mathbf{e}}, \tag{7}$$

where $\mathbf{e}$ is the error. k_p, k_i, k_d are proportional, integral and derivative gains, respectively. For a planar position control, $\mathbf{e}$ is a two dimensional vector and can be represented as

$$\mathbf{e} = \begin{bmatrix} x_{des} - x_{act} \\ y_{des} - y_{act} \end{bmatrix}. \tag{8}$$

Since magnet alignment is internally stable along the direction of the magnetic field at the location of the robot, we do not employ a closed-loop control strategy on the orientation. Instead, we set the direction of the magnetic field to match that of (θ_{des}.

Therefore, the actuation system presented in (6) is adapted as

$$\begin{bmatrix} \mathbf{B}_r \\ \mathbf{F}_m \end{bmatrix} = \begin{bmatrix} \bar{\boldsymbol{\beta}} \\ v_m \Psi_m^{\mathrm{T}} \bar{\mathbb{G}}_{\mathbf{x}}(\mathbf{P}) \\ v_m \Psi_m^{\mathrm{T}} \bar{\mathbb{G}}_{\mathbf{y}}(\mathbf{P}) \end{bmatrix} \begin{bmatrix} i_1 \\ i_2 \\ i_3 \\ i_4 \end{bmatrix} = \alpha_{B,F}(\mathbf{P})\mathbf{u_C}. \quad (9)$$

Solving this equation for the input currents to achieve desired force and robot alignment yields

$$\mathbf{u_C} = \begin{bmatrix} i_1 \\ i_2 \\ i_3 \\ i_4 \end{bmatrix} = \alpha_{B,F}(\mathbf{P})^{-1} \begin{bmatrix} \mathbf{B}_{\mathrm{des}} \\ \mathbf{u}_{\mathrm{d}} \end{bmatrix}. \quad (10)$$

$\mathbf{B}_{\mathrm{des}} = \|\mathbf{B}_{\mathrm{des}}\| [\begin{smallmatrix} \sin(\theta_{\mathrm{des}}) \\ \cos(\theta_{\mathrm{des}}) \end{smallmatrix}]$ is the vector along θ_{des} with a magnitude $\|\mathbf{B}_{\mathrm{des}}\|$. Because there is an order of magnitude difference in the magnetic field estimation between the dipole model and FEA-based simulations, the PID constants and θ_{d} have to be tuned separately. PID constants are used as $(k_p, k_i, k_d) = (0.4\frac{\mathrm{N}}{\mathrm{m}}, 0.1\frac{\mathrm{N}}{\mathrm{m.s}}, 0.025\frac{\mathrm{N.s}}{\mathrm{m}})$ and $(k_p, k_i, k_d) = (18\frac{\mathrm{N}}{\mathrm{m}}, 16\frac{\mathrm{N}}{\mathrm{m.s}}, 0.5\frac{\mathrm{N.s}}{\mathrm{m}})$ for dipole and FEA-based models, respectively. Similarly, $\|\mathbf{B}_{\mathrm{des}}\|$ is set to 25 mT for the dipole model and 3.75 mT for the FEA model.

B. Dipole vs. FEA-Based Model for Field Estimation

Having a closed-form mathematical solution for the magnetic field (and its spatial gradients) provides a strong tool for estimating the force and torque exerted on the robot for real-time closed-loop control applications, where fast computation is needed. Therefore, the dipole model has been a commonly used method for representing the magnetic field distribution at any desired location [22], [23]. For any electromagnetic field source with the dipole moment, $\bar{\mathbf{m}}_{\mathbf{s}}$, the magnetic field vector, $\bar{\mathbf{B}}$, at the location $\mathbf{P}$ can be calculated as

$$\bar{\mathbf{B}}(\bar{\mathbf{m}}_{\mathbf{s}}, \mathbf{P}) = \frac{1}{4\pi \|\mathbf{P}\|^3} \left[\frac{3(\bar{\mathbf{m}}_{\mathbf{s}} \cdot \mathbf{P})\mathbf{P}}{\|\mathbf{P}\|^2} - \bar{\mathbf{m}}_{\mathbf{s}} \right]. \quad (11)$$

The magnetic dipole model for unit currents will be evaluated at the robot's position, $\mathbf{P}$, to compute $\alpha_{B,F}$ and to solve for coil currents, $\mathbf{u_C}$ as in (10).

Since the dipole model reduces the finite three-dimensional electromagnetic coil geometry into a single point, it induces inaccuracies that are significant close to the coil. As an alternative and more accurate calculation approach, FEA methods could generate more accurate computation of the magnetic field by parsing the overall geometry into many small components instead of approximating the whole geometry as a single point. By assuming the quasi-stationary magnetic field of our system, the FEA computation is governed by Maxwell's equations and Gauss's Law

$$\nabla \times \mathbf{H} = \mathbf{J}, \quad (12)$$

$$\nabla \times \mathbf{E} = -\frac{\partial \mathbf{B}}{\partial t}, \quad (13)$$
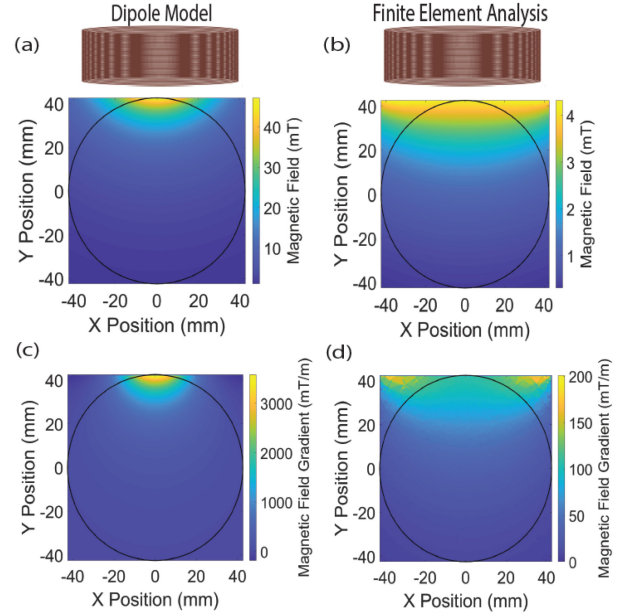
$$\nabla \cdot \mathbf{B} = 0 \quad (14)$$

Fig. 2. All the plots in this figure are for a unit current activation of the represented coil. The circle represents the Petri dish (region of interest). a-b) Magnetic field intensity using the dipole model and FEA results, respectively. c-d) Magnetic field gradient generated using the dipole model and FEA results, respectively.

where $\mathbf{H}$ is the magnetic field vector, $\mathbf{B}$ is the magnetic flux density vector, $\mathbf{E}$ is the electric field vector, and $\mathbf{J}$ is the volumetric current density vector. The constitutive equations for electric and magnetic fields are

$$\mathbf{J} = \sigma\mathbf{B}, \quad (15)$$

$$\mathbf{H} = \mu\mathbf{B}, \quad (16)$$

where σ and μ are the electrical conductivity matrix and the magnetic permeability matrix respectively. Because the coils are the source of magnetic field, $\mathbf{J}$ is represented as

$$\mathbf{J} = \frac{Ni}{A}, \quad (17)$$

where N is the number of coil turns, A is the total cross section area of the coil domain, and i is the input current of the coil. The magnetic field can be solved by discretizing the governing equations in the desired domains. We implemented the FEA computation of the magnetic field using COMSOL Multiphysics Version 5.5. The coil domain was discretized using 213,410 tetrahedron elements with a total mesh volume of 112,100 mm³, which provides good trade-off between computation accuracy and efficiency. Multifrontal Massively Parallel Sparse Direct Solver (MUMPS) is being used to solve the numerical problem.

Results of the FEA models along with the comparative dipole model magnetic fields in a 2D planar surface are provided in Fig. 2. The unit vector of the magnetic field direction is computed by taking the 2-norm of the magnetic field vector computed via magnetic dipole model and the FEA-based simulations. To acquire the ground truth, the magnetic field is measured with a gaussmeter (AlphaLab Inc., GM3) along a 10x9 grid with 8 mm
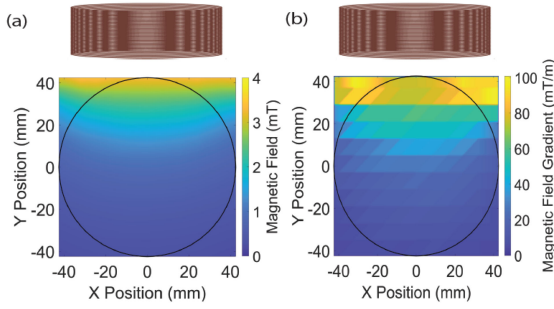
Fig. 3. Experimental characterization of (a) the magnetic field and (b) the magnetic gradient along the coil axis for a 1 A input current.
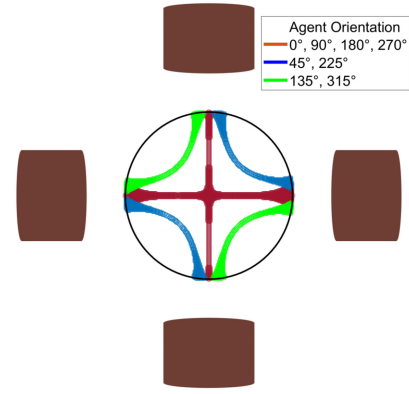

Fig. 4. Representation of singular locations in the Petri dish (region of interest), vary with the change in magnetic agent's orientation. Petri dish diameter is 85 mm. Electromagnetic coils on each sides are representative.

spatial discretization for a unit current. The magnetic field data is used to calculate magnetic gradient along the major axis. Both of these results are interpolated to provide a high-density color map. Interpolated results of the magnetic field ground truth data is provided in Fig. 3.

Our FEA-based magnetic model results are computed offline, stored, and accessed as a look-up table to maximize control loop rates. The resulting 2D data set is used to estimate the spatial distribution of the magnetic field in the workspace for a unit current in a coil. The magnetic field strength and the direction are extracted from the FEA model with a resolution of 0.5 mm as a 2D square grid. We use the magnetic field look-up values at the point of interest and its four neighbors in cardinal directions from each coil. The fields at neighboring points are utilized for gradient computations via first order numerical differentiation, $B_{diff}/2\,h$, where B_{diff} is the change of the magnetic field and h is the distance between grid points. To minimize the computation effort, curl-free magnetic field property assumption is implemented ($\partial B_x/\partial y = \partial B_y/\partial x$). The final results are used to compute the model-based scaling matrix, $\alpha_{B,F}(\mathbf{P})$, as previously shown in (9).

C. Magnetic Agent Localization and Discretization

We use optical camera images and image processing algorithms to track the magnetic agent. We use the U-net convolutional neural network architecture to train and segment out the agent localization data, as previously presented by Pryor *et al.* [16]. The output of the localization, $\mathbf{X}_{act} = [\,x_{act}\ y_{act}\ \theta_{act}\,]^{\mathrm{T}}$, is updated per frame ($\approx$20 Hz). To further increase the magnetic field estimation accuracy, the magnetic agent is discretized along its length. Since the magnetic agent has a finite volume, assumption of a single point at the center may not be sufficiently precise, especially for the locations where the agent is near a coil and field gradients are steep. Therefore, we discretize the magnetic agent along its length, generating 6 different voxels. The aforementioned computations for the magnetic field and gradients are computed for each voxel and added to form the resultant averaged $\alpha_{B,F}(\mathbf{P})$ matrix that is inverted to compute the desired coil currents. This averaged $\alpha_{B,F}(\mathbf{P})$ matrix for multiple voxels can be given as

$$\alpha_{B,F}(\mathbf{P}) = \sum_{k=1}^{v} \alpha_{B_k,F_k}(\mathbf{P_k}) \qquad (18)$$

where v is the number of discretized voxels (we use $v = 6$), $\mathbf{P_k}$ corresponds to the center position of each voxel location.

V. SINGULARITIES AND PATH GENERATION

Having the inverse of $\alpha_{B,F}$ as shown in (10) can lead to singularities for some poses of the magnetic agent shown in Fig. 4. In order to determine singularity, we look at the condition number of the $\alpha_{B,F}(\mathbf{P})$ matrix at each grid point in the petri-dish and for fixed magnetic agent orientation (resolution up to 1°) to see if it is more than a certain threshold (10^3). Such a situation typically results in the magnetic field changing abruptly, and therefore significant degradation in the magnetic agent steering quality is observed.

To demonstrate the improved control performance obtained using the FEA-based model over a dipole model, we design the trajectories far from the singular poses, while covering a large range of agent poses and movements. Additionally, since near-coil regions are more prone to modeling errors in dipole model estimation, some trajectories fully or partially remain in near-coil regions. Thus, we designed trajectories to show (P1) constant orientation (at 45° and 135°) with linear path tracking, (P2) constant orientation circular path tracking near the coils, (P3) constant position with pure rotation near the coils (for each of 4 coils), (P4) rotated square path centered on the origin with three different lengths, and (P5) circular path centered at the origin with three different diameters. For any given path, at any given time, t, $\mathbf{X}_{des}$ is computed as shown in (19).

$$\mathbf{X}_{des}(t) = \frac{(t - t_{i-1})}{(t_i - t_{i-1})}(\mathbf{W}_i - \mathbf{W}_{i-1}) + \mathbf{W}_{i-1}, \quad t \in (t_{i-1}, t_i) \qquad (19)$$

where $t_i = t_{i-1} + \|\mathbf{W}_i - \mathbf{W}_{i-1}\|/v_{des}$. $\mathbf{W}_0, \mathbf{W}_1, \mathbf{W}_2, \ldots,$ $\mathbf{W}_m$ are the sequence of position and orientation states on the desired path. v_{des} is the desired path-following velocity constant decided by the user. Path types (P1)–(P4) are performed far away from the singularity configurations. However, path (P5) experiences performance degradation due to the singularities when the orientation along the circle reaches to 0°, 90°, 180°, and 270°. These singular poses are represented in Fig. 4.
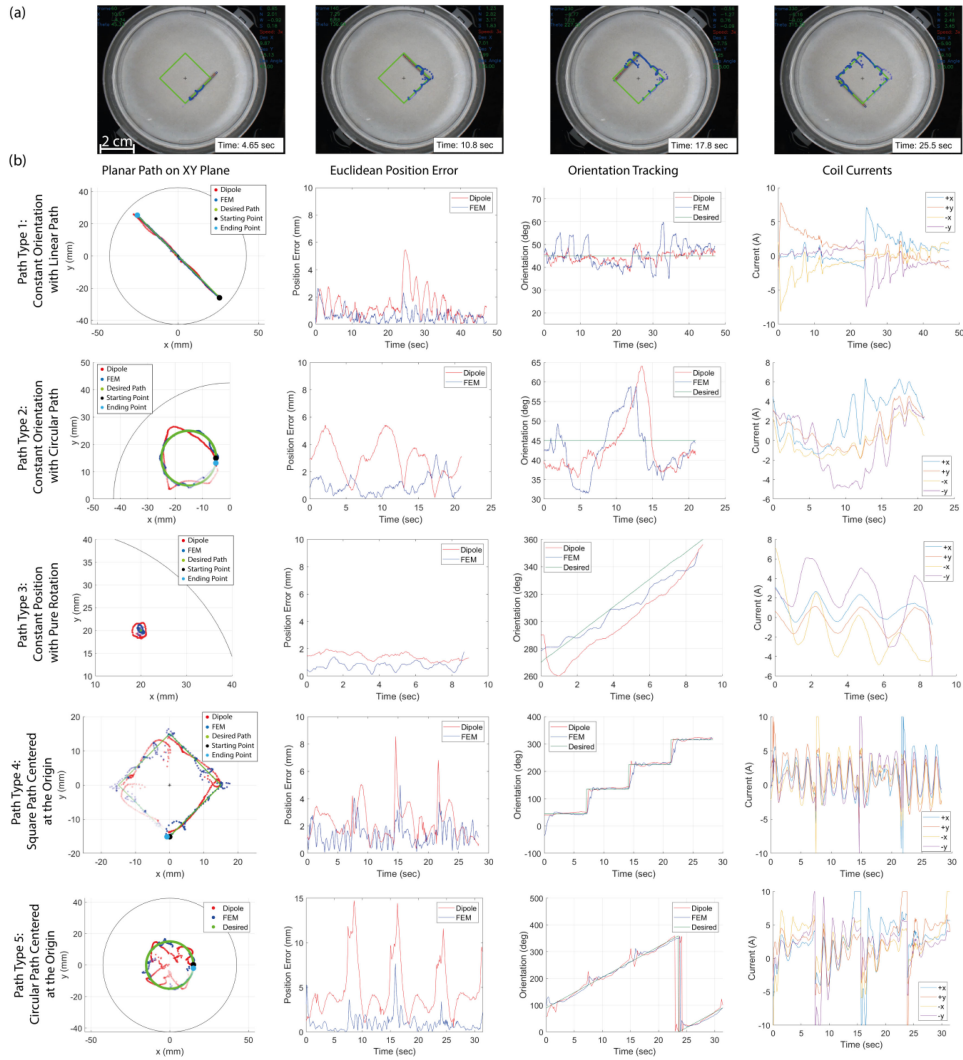
Fig. 5.   Among 5 trials for each path, the experiment with median position RMS error is presented. a) Representative sample of the experiments conducted (snapshots of the tracking of (P4) with an FEA-based magnetic model). b) Five different paths are implemented to compare the effect of modeling on the PID controller. The XY trajectory, time vs. position error, orientation (modulated in 0° - 360° range), and coil currents are provided in each column, from left to right, respectively.
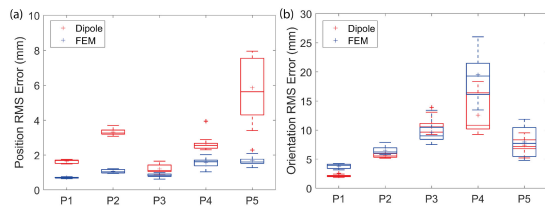

Fig. 6.   a) Comparative box-and-whisker plots for average position RMS errors for both magnetic models. b) Corresponding orientation RMS errors for the same experiments.

VI. COMPUTATIONAL COST

The closed-loop control system runs in a continuous loop, and its frequency is determined by the computational cost of the loop. Each loop consists of (1) image processing and localization, (2) closed-loop control algorithm, (3) magnetic model estimation, and (4) other computational costs such as realization of the

visualization markers and data storage. Closed-loop controller performance is dependent on the tracking rate, thus it is desired to have high rates.

Running FEA simulations in every loop cycle would drastically increase the computation time and negatively impact performance. To improve performance, we computed the FEA-based magnetic field offline and recorded the results in a two dimensional lookup table with 0.5 mm spatial resolution. In each cycle we can find the nearest measurement points to the current position and interpolate the magnetic field for a unit current. We analyzed the additional time cost that is introduced into our system due to our approach for estimating the magnetic fields.

VII. RESULTS

A. Path-Tracking Performances

Path-tracking performance for all path types with dipole model and FEA-based model are analyzed. We repeated the experiments 5 times for each path and the root-mean-square
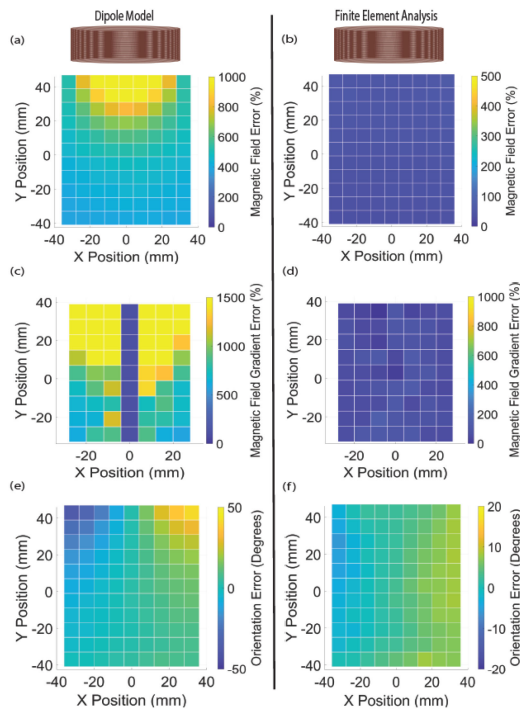
Fig. 7. All the plots in this figure are for a unit current activation of the represented coil. a-b) Normalized percentage error in the magnetic field strength between the dipole model and the FEA-based model. c-d) Normalized percentage error in the magnetic gradient along the axis of the coil between the dipole model and the FEA-based model. e-f) Absolute orientation error in the magnetic direction between the dipole model and the FEA-based model.

(RMS) errors presented will be the average RMS of each path type. Tracking performance for each of these five paths are provided in Fig. 5.

The average RMS errors as well as standard deviations of a total of 130 experiments are presented in Fig. 6. The FEA-based magnetic model case provides a better performance on the positioning of the magnetic agent compared to the dipole model case. In terms of orientation, both models show relatively close results. This is an expected outcome since the orientation is controlled in an open-loop fashion, and both the FEA-based magnetic model and the dipole magnetic model have relatively close agreement in terms of magnetic field direction, as shown in Fig. 7. All the paths except (P3) have less than 5° average orientation mismatch between the models. (P3) path average orientation mismatch is larger than 5°, and for this path, we observe 1.1° more accurate orientation control over the course of the path.

It is important to note that (P5) is the circular trajectory centered at the Petri dish center. This trajectory experiences singular points when the agent is on any of the cardinal axes and oriented along the axis of any of the coils. The dipole model results in a much larger positioning error under these singularities while the FEA-based model handles these singularity cases with less positioning error. Specifically, we observe 5.7 mm and 1.2 mm positioning RMS error for dipole and FEA-based models, respectively. For the dipole model case, the positioning errors for (P1), (P2), (P3), and (P4) are 1.8 mm, 3.3 mm, 1.2 mm, and 2.7 mm while the same errors for FEA-based model are 0.7 mm,

1.1 mm, 0.9 mm, 1.7 mm, respectively. The demonstration video provides the experimental recordings for each of the paths, where further details such as tracking speed can be observed.

B. Comparison Between Magnetic Models

The magnetic dipole model and FEA model are compared with the ground truth field measurement data presented in Fig. 3. The comparison results are presented in Fig. 7; experimental magnetic field measurements align significantly better with FEA model while providing orders of magnitude higher mismatch with the dipole model. The ground-truth comparison results indicate that the worst-case magnetic dipole model estimate is 1339% field error while FEA model worst-case estimate is 33% field error. This estimation error reduces to 425% and 21% in average throughout the overall workspace for dipole and FEA models, respectively. Similarly, more than 25x magnetic field gradient intensities are observed at near coil regions, which results in incorrect prediction of magnetic forces, which are about 25x larger than real-world physical values. While we observe orders of magnitude mismatches between the two magnetic field estimation models, the magnetic field orientation vector mismatch is less concerning. For the majority of the workspaces, the orientation mismatch is around 10° or less. For many points in the path tracking experiments, this orientation error remains less than 5°. The field measurements have small deviations depending on the probe's minor pose changes which may introduce minor characterization errors.

C. Computational Cost Analysis

The computation duration is another important metric. We calculated the average computational time for (1) localization, (2) controller, (3) magnetic model computations, and (4) other processes such as visualization and data savings. Recording these subroutine durations for 50 loop cycles, it is found that the average computational time for localization, controller, and other processes are 48 ms, 0.15 ms, and 1.8 ms, respectively. The average time and standard deviation for the computation of magnetic field model using the FEA model is 1.44 ms and 0.35 ms, respectively. The majority of 1.8 ms computation time is being utilized for interpolation between discrete grid points. The computation time required to estimate the magnetic field by using the magnetic dipole model is found to be an average of 0.37 ms with 0.2 ms standard deviation. The added computational time due to the proposed FEA-based magnetic model estimation is around 2% of the overall loop time, and hence, we have not observed a considerable degradation to the overall loop performance. The overall loop rate reduces from 19.88 Hz to 19.49 Hz. A visual representation of the computation times for each process are summarized in Fig. 8.

VIII. DISCUSSION AND CONCLUSION

We present a computation technique for realistic FEA models that generate accurate representation of the magnetic field generated in near-coil regions. Clinical version of the MagnetoSuture^{TM} system requires scaling-up in size, which
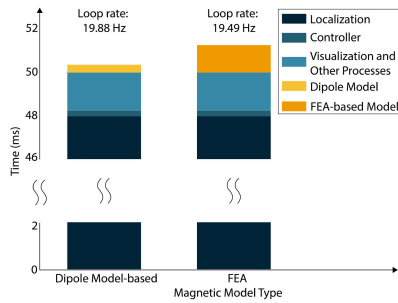
Fig. 8. The computational cost of the individual processes that are taking place sequentially in a typical system loop. The subroutines can be classified as localization, controller, magnetic model-related computations, and other processes such as visuals, data savings, inter-process communications. Adding the FEA-based model slightly increases the overall loop time. The resultant loop rate reduces from 19.88 Hz to 19.49 Hz.

would also enlarge 'inaccurate region' sizes. In addition, locating electromagnetic coils in reasonably close regions allow for generating stronger forces and torques while avoiding impractical electrical power ranges. Therefore, clinical magnetic needle steering systems would still be compact with larger coils, requiring more accurate magnetic modelling to prevent potential safety issues related to the estimation of magnetic force and torques on magnetic agents.

Our FEA-based magnetic model was tested on a PID controller, demonstrating controller improvement as compared with the dipole model-based field estimates. The orientation of the robot is controlled in an open-loop manner. Therefore, the orientation accuracy both in dipole and FEA models result in similar performances. Physical disturbances such as uneven surface contact, friction and drag forces, magnetic field estimation inaccuracies in both models, and magnet structure with a masking tape at the tip are some of the factors resulting in orientation inaccuracies.

The singular configurations can be avoided by adding more coils that create additional linearly independent field distributions [22]. In future work, hybrid control approaches and optimal coil powering strategies [24], [25] combined with precise magnetic model estimations will be implemented to avoid singular configurations and to provide high pose control accuracy towards ultra-precise magnetic surgeries. To reduce the computational costs, a partial or complete polynomial fits can be integrated. Since the controller performance degradation is related to the choice of the controller algorithm, the future studies will focus on comparing variety of nonlinear control techniques to demonstrate the relation between the controller algorithms and performance degradation under the presence of inaccurate field estimations. Additionally, we will develop imaging and localization with top and side cameras to extract 3D localization information of the robots along with the out-of-plane coils, which would lead to extending the proposed methodology for 3D manipulation tasks for closer relevance to the medical application requirements.

References

[1] G.-Z. Yang et al., "The grand challenges of science robotics," *Sci. Robot.*, vol. 3, no. 14, 2018, Art. no. eaar7650.

[2] M. Diana and J. Marescaux, "Robotic surgery," *J. Brit. Surg.*, vol. 102, no. 2, pp. e15–e28, 2015.

[3] Y. Fu, H. Liu, W. Huang, S. Wang, and Z. Liang, "Steerable catheters in minimally invasive vascular surgery," *Int. J. Med. Robot. Comput. Assist. Surg.*, vol. 5, no. 4, pp. 381–391, 2009. [Online]. Available: https://onlinelibrary.wiley.com/doi/abs/10.1002/rcs.282

[4] O. Erin et al., "Overcoming the force limitations of magnetic robotic surgery: Magnetic pulse actuated collisions for tissue-penetrating-needle for tetherless interventions," *Adv. Intell. Syst.*, vol. 4, 2022, Art. no. 2200072.

[5] Y.-L. Liu, D. Chen, P. Shang, and D.-C. Yin, "A review of magnet systems for targeted drug delivery," *J. Controlled Release*, vol. 302, pp. 90–104, 2019. [Online]. Available: https://www.sciencedirect.com/science/article/pii/S0168365919301919

[6] D. Son, H. Gilbert, and M. Sitti, "Magnetically actuated soft capsule endoscope for fine-needle biopsy," *Soft Robot.*, vol. 7, pp. 10–21, 2020.

[7] F. Carpi, N. Kastelein, M. Talcott, and C. Pappone, "Magnetically controllable gastrointestinal steering of video capsules," *IEEE Trans. Biomed. Eng.*, vol. 58, no. 2, pp. 231–234, Feb. 2011.

[8] L. O. Mair et al., "MagnetoSuture: Tetherless manipulation of suture needles," *IEEE Trans. Med. Robot. Bionics*, vol. 2, no. 2, pp. 206–215, May 2020.

[9] C. Pacchierotti et al., "Steering and control of miniaturized untethered soft magnetic grippers with haptic assistance," *IEEE Trans. Automat. Sci. Eng.*, vol. 15, no. 1, pp. 290–306, Jan. 2018.

[10] S. Yim, E. Gultepe, D. H. Gracias, and M. Sitti, "Biopsy using a magnetic capsule endoscope carrying, releasing, and retrieving untethered microgrippers," *IEEE Trans. Biomed. Eng.*, vol. 61, no. 2, pp. 513–521, Feb. 2014.

[11] C. Pappone et al., "Robotic magnetic navigation for atrial fibrillation ablation," *J. Amer. College Cardiol.*, vol. 47, no. 7, pp. 1390–1400, 2006.

[12] F. Carpi and C. Pappone, "Stereotaxis Niobe magnetic navigation system for endocardial catheter ablation and gastrointestinal capsule endoscopy," *Expert Rev. Med. Devices*, vol. 6, no. 5, pp. 487–498, 2009.

[13] S. Ernst, "Magnetic and robotic navigation for catheter ablation," *J. Interventional Cardiac Electrophysiol.*, vol. 23, no. 1, pp. 41–44, 2008.

[14] A. J. Petruska, J. Edelmann, and B. J. Nelson, "Model-based calibration for magnetic manipulation," *IEEE Trans. Magn.*, vol. 53, no. 7, pp. 1–6, Jul. 2017.

[15] M. Fan et al., "Towards autonomous control of magnetic suture needles," in *Proc. IEEE/RSJ Int. Conf. Intell. Robots Syst.*, 2020, pp. 2935–2942.

[16] W. Pryor et al., "Localization and control of magnetic suture needles in cluttered surgical site with blood and tissue," in *Proc. IEEE/RSJ Int. Conf. Intell. Robots Syst.*, 2021, pp. 524–531.

[17] S. Raval et al., "Magnetic model calibration for tetherless surgical needle manipulation using Zernike polynomial fitting," in *Proc. IEEE 21st Int. Conf. Bioinf. Bioeng.*, 2021, pp. 1–6.

[18] B. E. Kratochvil et al., "MiniMag: A hemispherical electromagnetic system for 5-DoF wireless micromanipulation," in *Experimental Robotics*, Berlin, Germany: Springer, 2014, pp. 317–329.

[19] A. Ghanbari, P. H. Chang, B. J. Nelson, and H. Choi, "Electromagnetic steering of a magnetic cylindrical microrobot using optical feedback closed-loop control," *Int. J. Optomechatronics*, vol. 8, no. 2, pp. 129–145, 2014.

[20] F. Ongaro, C. M. Heunis, and S. Misra, "Precise model-free spline-based approach for magnetic field mapping," *IEEE Magn. Lett.*, vol. 10, pp. 1–5, Nov. 2018.

[21] M. Etiévant, A. Bolopion, S. Régnier, and N. Andreff, "An improved control-oriented modeling of the magnetic field," in *Proc. Int. Conf. Robot. Automat.*, 2019, pp. 6178–6184.

[22] M. P. Kummer, J. J. Abbott, B. E. Kratochvil, R. Borer, A. Sengul, and B. J. Nelson, "OctoMag: An electromagnetic system for 5-DoF wireless micromanipulation," *IEEE Trans. Robot.*, vol. 26, no. 6, pp. 1006–1017, Dec. 2010.

[23] J. J. Abbott, E. Diller, and A. J. Petruska, "Magnetic methods in robotics," *Annu. Rev. Control Robot. Auton. Syst.*, vol. 3, pp. 57–90, 2020.

[24] R. Probst, J. Lin, A. Komaee, A. Nacev, Z. Cummins, and B. Shapiro, "Planar steering of a single ferrofluid drop by optimal minimum power dynamic feedback control of four electromagnets at a distance," *J. Magnetism Magn. Mater.*, vol. 323, no. 7, pp. 885–896, 2011.

[25] A. Pourkand and J. J. Abbott, "Magnetic actuation with stationary electromagnets considering power and temperature constraints," *IEEE Robot. Automat. Lett.*, vol. 5, no. 4, pp. 6964–6971, Oct. 2020.